

Controlled Coherent Coupling in a Quantum Dot Molecule Revealed by Ultrafast Four-Wave Mixing Spectroscopy

Daniel Wigger,^{1,2,*} Johannes Schall,³ Marielle Deconinck,³ Nikolai Bart,⁴ Paweł Mrowiński,^{1,5} Mateusz Krzykowski,¹ Krzysztof Gawarecki,¹ Martin von Helversen,³ Ronny Schmidt,³ Lucas Bremer,³ Frederik Bopp,⁶ Dirk Reuter,⁷ Andreas D. Wieck,⁴ Sven Rodt,³ Julien Renard,⁸ Gilles Nogues,⁸ Arne Ludwig,⁴ Paweł Machnikowski,¹ Jonathan J. Finley,⁶ Stephan Reitzenstein,³ Jacek Kasprzak^{6,8,*}

¹*Institute of Theoretical Physics, Wrocław University of Science and Technology, 50-370 Wrocław, Poland*

²*School of Physics, Trinity College Dublin, Dublin 2, D02 PN40, Ireland*

³*Institute of Solid State Physics, Technische Universität Berlin, 10623 Berlin, Germany*

⁴*Lehrstuhl für Angewandte Festkörperphysik Ruhr-Universität Bochum, 44780 Bochum, Germany*

⁵*Laboratory for Optical Spectroscopy of Nanostructures, Department of Experimental Physics, Wrocław University of Technology, 50-370 Wrocław, Poland*

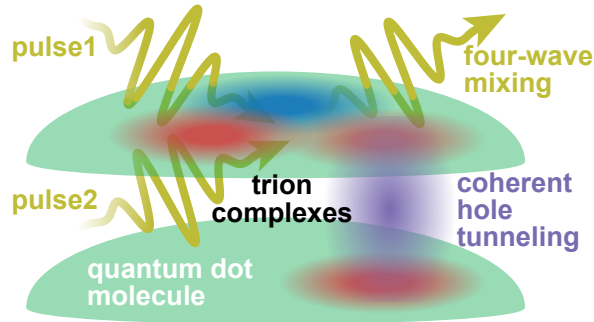
⁶*Walter Schottky Institut and Physik Department, Technische Universität München, 85748 Garching, Germany*

⁷*Department Physik, Universität Paderborn, 33098 Paderborn, Germany*

⁸*Université Grenoble Alpes, CNRS, Grenoble INP, Institut Néel, 38000 Grenoble, France*

**daniel.wigger@tcd.ie, jacek.kasprzak@neel.cnrs.fr*

Semiconductor quantum dot molecules are considered as promising candidates for quantum technological applications due to their wide tunability of optical properties and coverage of different energy scales associated with charge and spin physics. While previous works have studied the tunnel-coupling of the different excitonic charge complexes shared by the two quantum dots by conventional optical spectroscopy, we here report on the first demonstration of a coherently controlled inter-dot tunnel-coupling focusing on the quantum coherence of the optically active trion transitions. We employ ultrafast four-wave mixing spectroscopy to resonantly generate a quantum coherence in one trion complex, transfer it to and probe it in another trion configuration. With the help of theoretical modelling on different levels of complexity we give an instructive explanation of the underlying coupling mechanism and dynamical processes.



1 Introduction

Maintaining and controlling coherence of quantum states spanning multiple physically distinct systems is at the core of quantum technologies, like quantum information processing and communication [1] or quantum metrology [2]. In the competitive and multi-disciplinary quest for systems that might allow one to efficiently induce, control, and detect quantum coherence, exciton complexes in semiconductor quantum dots (QDs) were already very early recognized as promising building blocks [3, 4]. QDs offer an efficient light-matter interface [5], which makes it possible to control their quantum states at sub-picosecond timescales [6], beyond cryogenic temperatures up to ambient conditions [7].

Closely stacked QDs forming quantum dot molecules (QDMs) offer a large flexibility to control their optical and spin properties by external electric or magnetic fields [8, 9, 10, 11, 12, 13]. Therefore, they are particularly attractive for quantum applications, such as quantum repeaters, requiring efficient spin-photon interfaces. While spectral characteristics of the coupling have been revealed in QDM systems by linear spectroscopy methods [8, 9, 10, 11, 12, 13, 14], these experiments are only sensitive to the structure of eigenstates and their occupations, thus yielding a typical spectral picture that essentially characterizes two coupled modes of any kind, be it classical or quantum. In contrast, tracing coherences, which are fingerprints of quantum superpositions, requires the application of a coherent nonlinear spectroscopy tool, like four-wave mixing (FWM). This poses a major challenge, in particular in the case of single quantum systems, where the optical signal is very weak. For this reason, detecting coherent characteristics of the coupling between different excitonic complexes in self-assembled QDs is still in its infancy.

Fortunately, the epitaxial growth and nanoprocessing of QD-based quantum devices has been improved close to perfection and individual nanostructures can nowadays be embedded deterministically into advanced nanophotonic devices with high photon extraction efficiency to improve the application potential and to enable experiments relying on high single-photon flux [15, 16]. On the other hand, the development of heterodyning and interferometric techniques in FWM spectroscopy made it possible to apply this method to single quantum emitters and to detect and characterize the coupling between individual transitions in various systems [17, 18, 19, 20, 21, 22, 23].

Here, we go significantly beyond experiments on basic single structures by using QDMs with a much richer excitonic level scheme that can be controlled by an external bias. This allows us to demonstrate that the hole-tunnelling in the QDM can be used to transfer resonantly created quantum coherence between different trion transitions. Similar experiments were previously

performed on quantum wells [24, 25, 26, 27]. In contrast to those, a single QDM is an atomic-like system, which offers broader perspectives for quantum technologies, e.g., interfacing spins and photons, at the same time making the experiment much more challenging. This way we demonstrate the coherent control of coherences in a coupled QD system, as required for quantum applications [6]. We further show how this coherent coupling can be controlled by applying an electric field. In quantum optical terms, this amounts to parametrically switching between a V-system and a Λ -system in a single physical structure, which allows us to address different pairs of coherences.

Through this first demonstration we make a crucial step toward the implementation of the ultrafast FWM methodology in photonic quantum technologies. In this way our work paves the way toward the realization of controlled long-range coherent coupling between distant solid state qubits.

2 Device and experimental method

We here use the aforementioned advantages of semiconductor quantum photonic technology to demonstrate controlled coherent coupling between excitonic transitions hosted by a pair of InAs QDs separated by ≈ 8 nm, forming a QDM [8, 9, 14, 16]. The system is doped, so that, apart from spin degeneracy, the ground state manifold of the QDM consists of two states, with a hole in one or the other QD, as schematically depicted in Fig. 1(a). As seen in the sketch in Fig. 1(b), from the two coupled charged three-particle complexes (trions) that can be excited optically, one is entirely located in one of the QDs, while the other spans both dots. We prove the coupling between the optically induced coherences between these hole and trion states in the coupled QDM system by performing two-dimensional four-wave mixing (2D FWM) spectroscopy (see below), in which coherent coupling between different optically active transitions is revealed as off-diagonal peaks in the 2D spectra [23]. Similar results can be expected for exciton transitions in the other QD, which are typically separated by several meV and are therefore not accessible in this study due to the limited spectral width of the excitation [13].

In our sample, the QDMs are placed in the structure schematically shown in Fig. 1(c), the layer structure of this QDM quantum device supports storage of holes by an AlGaAs tunneling barrier between the QDMs and the p-doped region of the diode. To achieve suitably high optical in- and out-coupling efficiency for the FWM signal [21], a circular Bragg grating is deterministically positioned around the QDM in the center of the quantum device. For details on the sample design and processing we refer to Ref. [16]. The charge-doped layers surrounding the

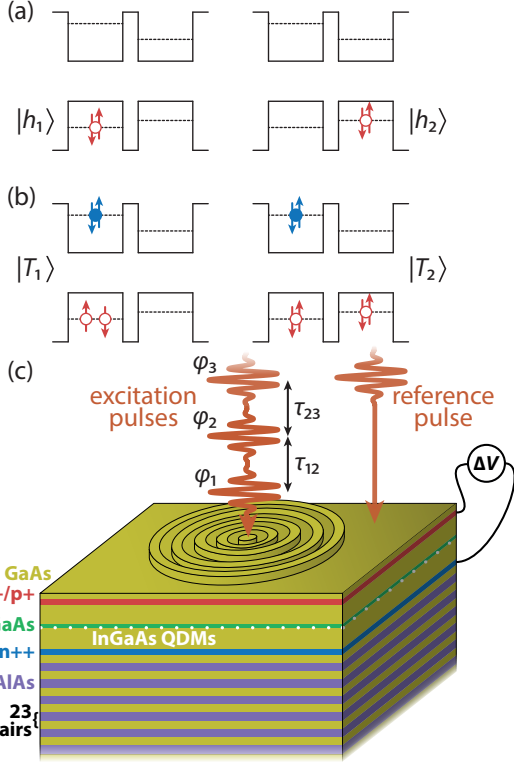


Figure 1: Involved QDM states and experimental setup. (a) Ground states of the involved trions possessing one hole in either of the quantum dots. (b) Relevant excited states formed by an additional exciton in the left quantum dot. (c) Schematic picture of the sample structure. Above a GaAs/AlAs distributed Bragg reflector the InGaAs quantum dot molecule (QDM) layer is sandwiched between charge-doped layers, which are connected to a bias source. The optical in- and out-coupling is improved by a circular Bragg grating, also called a bulls-eye photonic structure, on the top surface. The laser pulses used for the optical excitation in the four-wave mixing experiment are focused on the center of the grating, while the reference beam hits the free surface in the vicinity.

QDM sheet provide a p-i-n diode structure allowing voltage control. While scanning the external bias voltage, we monitor the formation of off-diagonal peaks in 2D FWM spectra of the molecule.

3 Results

Photoluminescence spectra

For characterising the QDM's optical properties we measure photoluminescence (PL) spectra for varying applied electric fields, which leads to an energy shift of the involved electronic states with respect to each other. Consequently, the hole and

trion states in the two dots are brought into resonance for specific electric fields and the tunnel-coupling leads to characteristic avoided crossings in the optical spectra. The results of this pre-characterisation are depicted in Fig. 2(a) and are in excellent agreement with the findings in Ref. [16]. To further check the integrity of the emitter structure we calculate the transition energies for a heuristic, semi-empirical model of the QDM as shown by the dashed lines (details are given in the Supporting Information (SI)). We use the same fitting parameters as in Ref. [16] and achieve the same high level of agreement with the measured spectral lines. Note, that not all possible transitions from the rich spin configurations including singlet and triplet states predicted by the theory (dashed lines) appear as bright spectral lines in the measurement because their dipole matrix elements are small and the optical signal is not visible at the given signal-to-noise ratio. While the entire structure of the PL spectra is quite complex with a total of ten visible lines, we are particularly interested in the four pronounced avoided crossings, which indicate state hybridisations and coherent tunnel-couplings. Two avoided crossings appear around an applied bias of $\Delta V \approx -650$ mV and are attributed to the resonance between the two hole states (ground states). The other two at

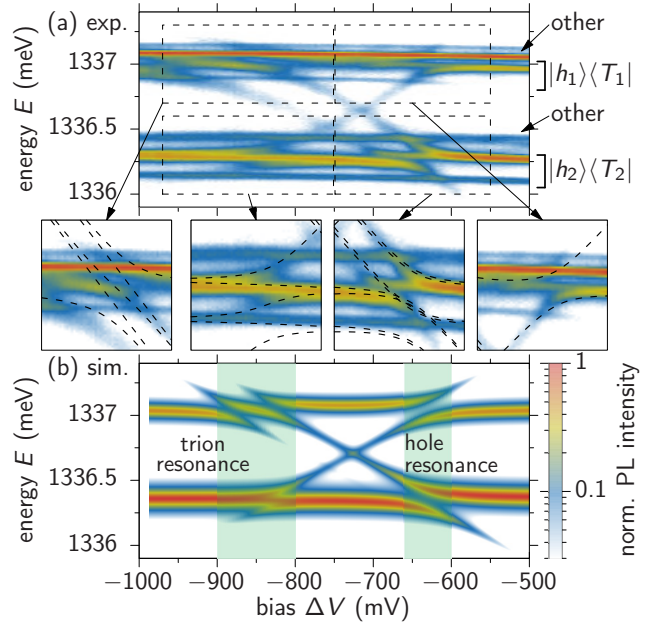


Figure 2: Bias scan of the PL spectra of the QDM-device. (a) Measured PL spectra as a function of the applied bias. The labels on the right mark the respective trions correspond to Fig. 5(a) and transitions from other exciton complexes, likely neutral excitons. The zoom-ins show the calculated optical transitions as dashed lines. (b) Semi-empirical simulation of the PL spectrum. The avoided crossings marked by the green shaded areas on the left stem from trion (excited state) resonances, those on the right from hole (ground state) resonances.

$\Delta V \approx -850$ mV stem from the resonance of the trion states (excited states). We also find other bright spectral lines that are unaffected by the applied electric field and do not participate in the avoided crossings (marked by 'other'). These transitions likely belong to neutral excitons in the QDM (SI).

In Fig. 2(b) we show simulated PL spectra derived from a semi-empirical model [28, 29] (SI) leading to the dashed lines in the zoom-ins in (a). Due to the optical selection rules we find that not all transitions lead to bright emission lines in the spectrum (SI). The brightest lines, which form avoided crossings, are well reproduced by the simulation. In order to relate the spectra to the morphological characteristics of the QDM and to confirm the form of the spectrum with a model based on realistic wave functions and an extended number of hole and trion states, we have performed $\mathbf{k} \cdot \mathbf{p}$ calculations [30, 31, 32, 33, 34, 35, 36, 37, 38, 39, 40, 41] of the trion PL spectra. In spite of the multiple transitions present in the $\mathbf{k} \cdot \mathbf{p}$ model, the low-excitation PL spectrum is very similar to that obtained in the semi-empirical model (SI).

Although the line splittings in the PL spectra certainly stem from the coupling between the two different exciton complexes, the appearance of an avoided crossing can be described already by a classical coupled oscillator model. Therefore, our goal is to directly address quantum coherence properties of the coupling mechanism via FWM micro-spectroscopy. In this experiment the QDM is resonantly excited with three laser pulses $\mathcal{E}_{1,2,3}$ (see Fig. 1(c) and SI). Each of the pulses is phase-labeled by $\mathcal{E}_{1,2,3} \sim e^{i\varphi_{1,2,3}}$, which can experimentally be achieved by different propagation directions $\mathbf{k}_{1,2,3}$ [42] or – as in our case – by radio frequency-shifts $(\Omega_1, \Omega_2, \Omega_3) = (80, 79, 79.77)$ MHz [17]. The considered FWM signal is then carried by the phase combination $\varphi_3 + \varphi_2 - \varphi_1$ [43, 44], which means that, at small pulse areas, we are detecting the third-order nonlinearity $\sim \mathcal{E}_1^* \mathcal{E}_2 \mathcal{E}_3$ ($\chi^{(3)}$ regime). This FWM signal from the sample is retrieved via a heterodyne detection with a reference pulse that is focused next to the grating structure on the sample surface (Fig. 1(c)). As explained in more detail below, the first pulse resonantly creates trion quantum coherences, which are transferred to the other trion states by tunnel-coupling and the second and third pulse. The FWM signal is then emitted with respectively different energies. By varying the delay between the first and second pulse τ_{12} and keeping $\tau_{23} = 0$ fixed, we are able to probe the coherence dynamics in the system (SI). Note, that this method directly probes the quantum coherence between the involved optically active states and therefore immediately demonstrates the quantum nature of the observed avoided crossing. Besides the coherent coupling, this spectroscopy method goes well beyond conventional (μ PL) spectroscopy and can give valuable insight in the homogeneous broadening [45, 46], phonon-induced dephasing processes [47], or

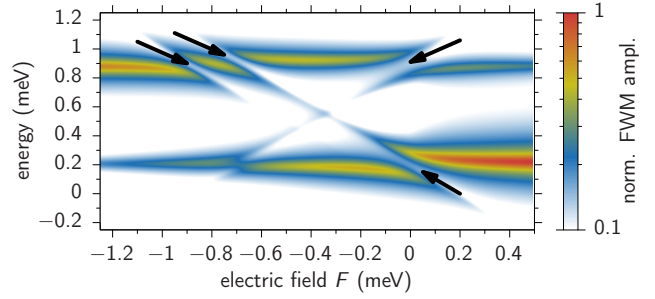


Figure 3: Simulated bias scan of the FWM spectrum of the QDM corresponding to the dashed lines in Fig. 2(a). The arrows mark the clear avoided crossings.

Rabi oscillations [43]. Moreover, by changing the pulse powers we can characterise the light-matter coupling strength [48] (SI).

Four-wave mixing spectra

To get a first expectation for the avoided crossing behaviour in FWM, we apply the model used to describe the PL spectra in Fig. 2 and calculate the FWM spectra for ultrafast laser pulses in the δ -pulse limit depicted in Fig. 3, where we consider vanishing pulse delays $\tau_{12} = \tau_{23} = 0$ and a dephasing rate of $\gamma = 0.05$ meV. Note, that the electric field is here given as energy shift between the lowest hole states in the two dots. We also calculated corresponding spectra by solving the Lindblad equation considering a non-vanishing pulse duration of $\Delta t = 0.2$ ps and achieved a very similar result (SI). Here, we find the same structure of avoided crossings as marked by the arrows. The lower energy one at $F \approx -0.75$ meV is bridged by a spectral line, such that one avoided crossing remains at $F = 0$ meV. In the higher energetic transitions we find three clear gaps in the spectrum (arrows), two around $F \approx -0.75$ meV and the other at $F = 0$ meV. In addition, the intensity distribution of the different lines has to be addressed. Due to the thermal occupation ($T = 7$ K, as in the experiment) of the two ground (hole) states before any optical excitation, the resulting intensities depend on which of the QDs has the lowest hole state energy for a given applied electric field. This finally results in brighter FWM lines at lower energies for larger bias values and in higher intensities at larger transition energies for smaller bias values. The visibility of the crossing lines around $F = -0.4$ meV [$\Delta V \approx -730$ mV in Fig. 2(b)] is significantly reduced in FWM compared to PL (Fig. 2(b)). This happens because of the nonlinear character of the signal in the $\chi^{(3)}$ regime, which suppresses transitions with weaker dipole matrix elements.

In Fig. 4(a) we show the respective measured bias scan of the FWM spectra for small pulse delays $\tau_{12} = \tau_{23} = 0.1$ ps which

maximize the FWM response and can still be treated as $\tau_{12} = \tau_{23} = 0$ in the simulation. Note, that the depicted bias range differs from the PL measurement in Fig. 2(a). The reason is that the state energies strongly depend on the optical excitation conditions (see SI for details). Therefore, the bias ranges in PL and FWM cannot be compared directly. The lowest energetic line stems from a neutral exciton. Therefore, it involves different charge states of the system and does not interact with the trion transition lines. We thus use it to phase-correct the delay scans, to generate 2D FWM spectra (see Fig. 4(b, c) and SI). The upper two spectral lines clearly belong to the trion transitions we are interested in. Obviously, much fewer spectral features are visible compared to the measured PL spectra [Fig. 2(a)], which is again related to the fact that the FWM signal is nonlinear and stems from the $\chi^{(3)}$ response of the optical transitions. Therefore, one naturally expects spectral lines that are weaker in PL to be strongly suppressed in FWM. Consequently, they might drop below the signal-to-noise level and do not appear in the detected spectra. Nevertheless, by comparing the measurement in Fig. 4(a) with the simulation in Fig. 3 we find striking similarities. First of all, we observe the same intensity distribution with stronger low-energy lines at larger electric fields ($\Delta V \approx -200$ mV) and stronger high-energy lines at smaller electric fields ($\Delta V \approx -450$ mV). We also see one small indication of an avoided crossing in the low-energy line at $\Delta V \approx -300$ mV (\nwarrow arrow), while no such feature appears in this spectral line at smaller fields. We further find a few indications of avoided crossings in the transition line at higher energies. Although only slightly above the noise-level, we can identify three gaps in the spectral line, namely at $\Delta V = -390$, -360 (\searrow arrows), and -300 mV (\swarrow arrow). These observations are in agreement with the predictions from the model in Fig. 3. Our $\mathbf{k} \cdot \mathbf{p}$ model with an extended electron and hole state basis and a QDM morphology mapped – as far as possible – from a typical grown QDM structure yields FWM spectra that exhibit exactly the same features. It shows two horizontal branches interrupted by avoided crossings, and their intensities decay in the opposite bias directions and no additional transitions are visible (SI). This validates the applicability of the semi-empirical model, but may open the path to study the effect of composition and morphology on the nonlinear optical response and quantum coherence properties of the QDM.

We move forward to the main result, which is the demonstration and control of the quantum coherence transfer between different trion complexes in the QDM. The bias-controlled coherent coupling of the QDM is revealed by measuring 2D FWM spectra, as exemplarily depicted in Figs. 4(b, c). The two energy axes of these 2D spectra are on the one hand determined by the spectrometer in the emitted signal (horizontal, E) and on the other hand by a Fourier transform with respect to the delay

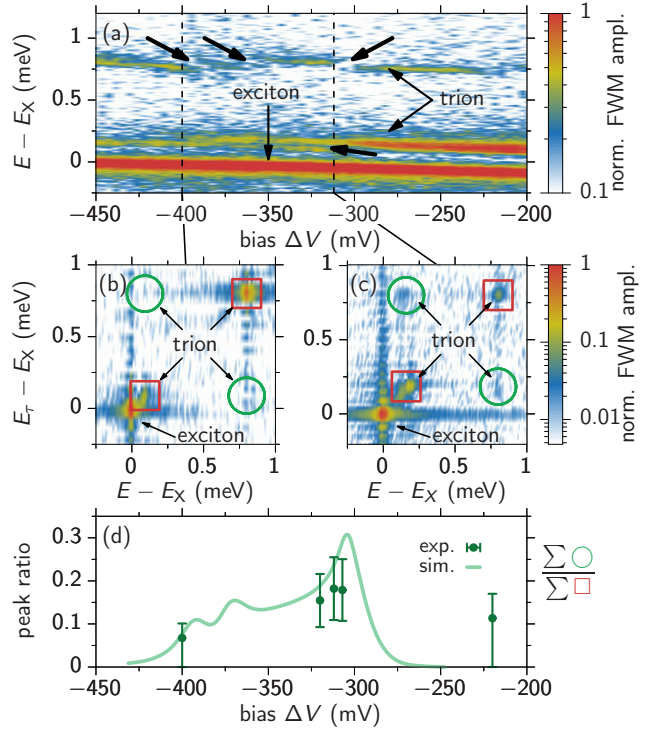


Figure 4: (a) Measured bias scan of the QDM FWM spectra with pulse delays $\tau_{12} = \tau_{23} = 0.1$ ps. The arrows correspond to those in Fig. 3(b). (b, c) Exemplary 2D FWM spectra at the bias values marked in (a). Red boxes mark the diagonal peaks and green circles the off-diagonal peaks used to determine the peak ratios in (c). (d) Peak ratios in the 2D FWM spectra to quantify the coherent coupling as a function of applied bias. Experiment as dots and simulation as line with homogeneous and inhomogeneous dephasing rates $\gamma = 0.05$ meV and $\sigma = 0.15$ meV, respectively.

τ_{12} in the FWM measurement (vertical, E_τ). The meaning of the different peaks in the maps can directly be read from the plots: Optical absorption and FWM emission from the same trion is represented by the peaks on the diagonal of the plot (red squares). Off-diagonal peaks, at the positions marked by the green circles, stem from an optical absorption from one trion (E_τ axis) and FWM generation from another one (E axis), due to their coherent tunnel-coupling. Therefore, the presence of these peaks in Fig. 4(c) confirms the coherent quantum state transfer for the electric field, where the two hole/ground states are in resonance ($\Delta V \approx -300$ mV). We see that the off-diagonal peaks are suppressed in Fig. 4(b) ($\Delta V = -400$ mV), indicating a much less efficient coherence transfer for electric fields where the excited states are not in close resonance.

Despite the limited signal-to-noise ratio of the 2D spectra, which makes a consistent quantitative analysis challenging, we carefully determine the relative strength of the off-diagonal peaks with respect to the diagonal ones, and therefore quantify the

coherent coupling between the QDs. Special attention has to be paid to disregard the impact of the dominant neutral exciton peak, marked in the plots (SI). We then determine the peak visibility by calculating the ratio of the sum-intensity of the off-diagonal peaks with respect to the diagonal ones, as symbolically written next to Fig. 4(d). In this figure the peak ratios from the performed experiments are shown as green dots and the corresponding simulation as pale green curve. For the simulation we consider a similar spectral broadening as in Fig. 3 (SI). Both, experiment and theory show increased peak ratios around the avoided crossing at a bias of $\Delta V \approx -300$ mV and the measurement and the simulation show a reasonable agreement. Note, that to match the experiment we have to assume additional inhomogeneous dephasing due to fluctuations of the transition energies with a standard deviation of $\sigma = 0.15$ meV (see SI for details) [46]. In short, an additional dephasing of the cross-coherences $|T_{2,1}\rangle\langle h_{1,2}|$, exceeding the pure dephasing acting on the optical active coherences $|T_{1,2}\rangle\langle h_{1,2}|$, will reduce the visibility of the off-diagonal peaks in the 2D spectrum. Such an additional dephasing is expected for coherences between states differing in charge distribution due to their large sensitivity to environmental fluctuations.

Minimum model interpretation

To fully understand the transfer of the coherence between the trions in the FWM process we developed a minimum model that only considers one ground hole state per QD ($|h_{1,2}\rangle$) and the corresponding bright trion states with an additional electron-hole pair in one of the dots ($|T_{1,2}\rangle$), which makes a total of four levels similar to Ref. [25, 27]. A schematic of the coupling mechanisms between these states is depicted in Fig. 5(a). While optical excitations $\mathcal{E}_{T1,T2} = \mathcal{E}(t)M_{T1,T2}$ are only possible within each trion complex (T1, T2, vertical connection), the tunnelings $t_{h,T}$ connect the hole (h) and trion (T) states (horizontal connection), respectively. This system can be described by the Hamiltonian:

$$\begin{aligned}
 H = & pF |h_2\rangle\langle h_2| + E_1 |T_1\rangle\langle T_1| + (pF + E_2) |T_2\rangle\langle T_2| \\
 & + \mathcal{E}_{T1}^*(t) |h_1\rangle\langle T_1| + \mathcal{E}_{T1}(t) |T_1\rangle\langle h_1| \\
 & + \mathcal{E}_{T2}^*(t) |h_2\rangle\langle T_2| + \mathcal{E}_{T2}(t) |T_2\rangle\langle h_2| \\
 & + t_h(|h_1\rangle\langle h_2| + |h_2\rangle\langle h_1|) + t_T(|T_1\rangle\langle T_2| + |T_2\rangle\langle T_1|).
 \end{aligned}$$

When we now assume that the two hole states are in resonance we can neglect the tunneling between the trion states, because they are far from resonance ($t_T = 0$). This situation is schematically shown in Fig. 5(b, left) where the tunnel coupling between the hole states leads to a hybridisation resulting in a new upper $|g_u\rangle$ and lower ground state $|g_l\rangle$ (middle). The optical active transitions now connect both of these states to each trion state resulting in a V-level structure. To construct the FWM

signals with the phase combination $\varphi_3 + \varphi_2 - \varphi_1$ we consider the two double-sided Feynman diagrams on the right. We see that the V-level structure induced by the hole tunnelling results in different possibilities to have an absorption in $|T_1\rangle$ and an emission in $|T_2\rangle$ (the other off-diagonal peak is retrieved by exchanging 1 and 2). The 1st diagram reaches the coherence transfer between the two trion complexes via the ground state doublet $|g_l\rangle\langle g_{ij}|$ after φ_2 and the 2nd one via the inter-trion coherence $|T_2\rangle\langle T_1|$. It is interesting to note, that coherent coupling is mediated via the common ground states where the hole states are de-localised across the two dots, but in the trion states the hole states are localised in each dot. The lifted degeneracy of the ground states in theory leads to the generation of multiple peaks on the off-diagonal, which cannot be resolved in the experiment but are visible in the simulated 2D spectra in the SI. An equivalent situation is found when the trion states are in resonance forming new excited states $|X_{u,l}\rangle$ resulting in an Λ -level scheme as depicted in Fig. 5(c). Here, the initial state is a thermal mixture of the hole states $|h_1\rangle$ and $|h_2\rangle$ and the Feynman diagrams show that the path of coherence transfer goes via

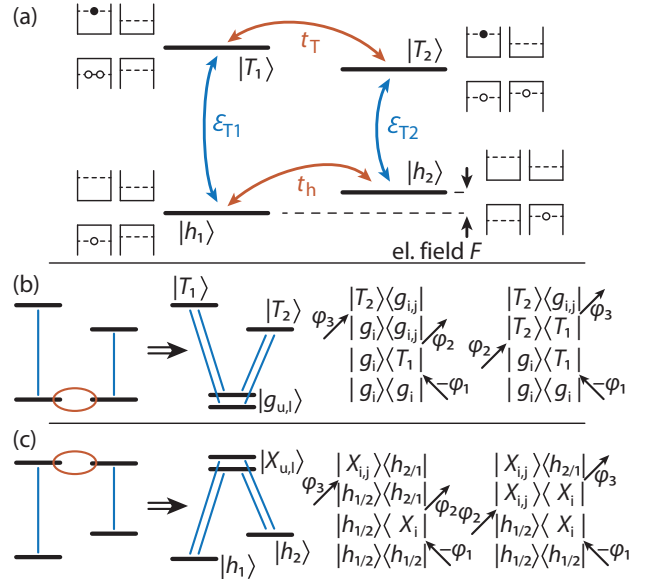


Figure 5: (a) Schematic picture of the minimum model to explain the coherent coupling effect. We include two hole $|h_{1,2}\rangle$ and two trion states $|T_{1,2}\rangle$ in the two QDs as depicted next to each level. We consider an optical transitions $\mathcal{E}_{T1,T2}$ (blue) and tunnel couplings between the hole and the trion states (orange). (b, c) Illustration of the hole (b) and trion resonances (c). Left: Exciton level structure with optical transitions (blue lines) and tunnel coupling (orange ellipses). Middle: New eigenstates forming ground $|g_{u,l}\rangle$ (b) and excited states $|X_{u,l}\rangle$ (c) doublets of upper (u) and lower (l) states. Right: Relevant double-sided Feynman diagrams leading to the off-diagonal (coherent coupling) peaks in the 2D spectra with $i, j = u, l$.

the hole states $|h_1\rangle\langle h_2|$ or the excited states doublet $|X_u\rangle\langle X_l|$ to the respective other hole state.

Before the FWM pulse sequence is started, the QDM is typically in its ground states, i.e., in a thermal equilibrium of the hole states. However, recently an experimental scheme has been developed to deterministically initialise the QDM in one of the two hole states [49]. It is thus becoming possible to induce a uni-directional coherence transfer between the two QDs. This would manifest in the 2D FWM spectrum with the appearance of only one off-diagonal peak. One would be starting from a non-eigenstate of the system which introduces additional dynamics in the system. It is important to note, that this FWM scheme offers the possibility to probe different coherence dynamics that are not optically active, namely $|g_u\rangle\langle g_l|$, $|h_1\rangle\langle h_2|$, $|X_u\rangle\langle X_l|$, and $|T_1\rangle\langle T_2|$. To achieve this one would have to vary the delay between the 2nd and 3rd pulse (τ_{23}) as can be seen from the Feynman diagrams in Fig. 5(b, c).

4 Conclusions

In summary, revealing controlled coherent coupling between different trion complexes in a QDM renders a major advance in the field of photonic quantum technology. Our proof-of-principle demonstration of nonlinear multi-wave mixing spectroscopy on these systems opens the door to address coherences that are not optically active, making them significantly longer lived than their bright counterparts, and could therefore be used as quantum storage [25, 27]. To improve the performance of quantum devices, current work aims to generate singlet-triplet qubits [50, 51, 52], which are expected to be robust against decoherence from electrostatic and magnetic fluctuations in the solid. Due to its selective access to different quantum coherences, the FWM method stands out as an excellent tool to exploit this new benchmark for quantum computing with solid state qubits.

Acknowledgements

D.W. thanks the Polish National Agency for Academic Exchange (NAWA) for financial support within the ULAM program (Grant No. PPN/ULM/2019/1/00064) and the Science Foundation Ireland (SFI, Grant No. 18/RP/6236). J.K. acknowledges the support from MCQST and Global Invited Professorship at the TU Munich and 'Tandem for Excellence' IDUB scheme at the University of Warsaw. P.Mr., M.K., K.G., C.D., F.B., J.J.F. and P.Ma. acknowledge support from the Polish National Science Centre (NCN) (Grant No. 2016/23/G/ST3/04324). The Berlin team acknowledge support by the German Federal

Ministry of Education and Research (BMBF) through the projects Q.Link.X and QR.X. We thank Thilo Hahn for helpful comments regarding inhomogeneous broadening.

References

1. Horodecki, R., Horodecki, P., Horodecki, M. & Horodecki, K. Quantum entanglement. *Rev. Mod. Phys.* **81**, 865–942 (2009).
2. Giovannetti, V., Lloyd, S. & Maccone, L. Advances in quantum metrology. *Nat. Photonics* **5**, 222–229 (2011).
3. Henneberger, F. & Benson, O. *Semiconductor quantum bits* (CRC Press, 2016).
4. Michler, P. *Quantum dots for quantum information technologies*, vol. 1 (Springer, 2017).
5. García de Arquer, F. P. *et al.* Semiconductor quantum dots: Technological progress and future challenges. *Science* **373**, eaaz8541 (2021).
6. Fras, F. *et al.* Multi-wave coherent control of a solid state single emitter. *Nat. Photonics* **10**, 155 (2016).
7. Holmes, M. J., Choi, K., Kako, S., Arita, M. & Arakawa, Y. Room-temperature triggered single photon emission from a III-nitride site-controlled nanowire quantum dot. *Nano Lett.* **14**, 982–986 (2014).
8. Bayer, M. *et al.* Coupling and entangling of quantum states in quantum dot molecules. *Science* **291**, 451–453 (2001).
9. Krenner, H. J. *et al.* Direct observation of controlled coupling in an individual quantum dot molecule. *Phys. Rev. Lett.* **94**, 057402 (2005).
10. Doty, M. F. *et al.* Electrically tunable g factors in quantum dot molecular spin states. *Phys. Rev. Lett.* **97**, 197202 (2006).
11. Doty, M. F. *et al.* Optical spectra of doubly charged quantum dot molecules in electric and magnetic fields. *Phys. Rev. B* **78**, 115316 (2008).
12. Kim, D. *et al.* Optical spin initialization and nondestructive measurement in a quantum dot molecule. *Phys. Rev. Lett.* **101**, 236804 (2008).
13. Ardel, P.-L. *et al.* Coulomb mediated hybridization of excitons in coupled quantum dots. *Phys. Rev. Lett.* **116**, 077401 (2016).

14. Stinaff, E. A. *et al.* Optical signatures of coupled quantum dots. *Science* **311**, 636 (2006).
15. Rodt, S., Reitzenstein, S. & Heindel, T. Deterministically fabricated solid-state quantum-light sources. *J. Phys. Condens. Matter* **32**, 153003 (2020).
16. Schall, J. *et al.* Bright electrically controllable quantum-dot-molecule devices fabricated by in situ electron-beam lithography. *Adv. Quantum Technol.* **4**, 2100002 (2021).
17. Langbein, W. & Patton, B. Heterodyne spectral interferometry for multidimensional nonlinear spectroscopy of individual quantum systems. *Opt. Lett.* **31**, 1151 (2006).
18. Martin, E. W. & Cundiff, S. T. Inducing coherent quantum dot interactions. *Phys. Rev. B* **97**, 081301(R) (2018).
19. Kasprzak, J., Patton, B., Savona, V. & Langbein, W. Coherent coupling between distant excitons revealed by two-dimensional nonlinear hyperspectral imaging. *Nat. Photonics* **5**, 57–63 (2011).
20. Raymer, M. G., Marcus, A. H., Widom, J. R. & Vitullo, D. L. P. Entangled photon-pair two-dimensional fluorescence spectroscopy (EPP-2DFS). *J. Phys. Chem. B* **117**, 15559–15575 (2013).
21. Mermillod, Q. *et al.* Harvesting, coupling, and control of single-exciton coherences in photonic waveguide antennas. *Phys. Rev. Lett.* **116**, 163903 (2016).
22. Mermillod, Q. *et al.* Dynamics of excitons in individual InAs quantum dots revealed in four-wave mixing spectroscopy. *Optica* **3**, 377 (2016).
23. Delmonte, V. *et al.* Coherent coupling of individual quantum dots measured with phase-referenced two-dimensional spectroscopy: Photon echo versus double quantum coherence. *Phys. Rev. B* **96**, 041124(R) (2017).
24. Davis, J. A. *et al.* Three-dimensional electronic spectroscopy of excitons in asymmetric double quantum wells. *J. Chem. Phys.* **135**, 044510 (2011).
25. Langer, L. *et al.* Magnetic-field control of photon echo from the electron-trion system in a CdTe quantum well: Shuffling coherence between optically accessible and inaccessible states. *Phys. Rev. Lett.* **109**, 157403 (2012).
26. Nardin, G. *et al.* Coherent excitonic coupling in an asymmetric double ingaas quantum well arises from many-body effects. *Phys. Rev. Lett.* **112**, 046402 (2014).
27. Salewski, M. *et al.* High-resolution two-dimensional optical spectroscopy of electron spins. *Phys. Rev. X* **7**, 031030 (2017).
28. Ponomarev, I. V. *et al.* Theory of spin states in coupled quantum dots. *Phys. Stat. Sol. (b)* **243**, 3869–3873 (2006).
29. Scheibner, M. *et al.* Spin fine structure of optically excited quantum dot molecules. *Phys. Rev. B* **75**, 245318 (2007).
30. Bahder, T. B. Eight-band $\mathbf{k}\cdot\mathbf{p}$ model of strained zinc-blende crystals. *Phys. Rev. B* **41**, 11992 (1990).
31. Winkler, R. *Spin-Orbit Coupling Effects in Two-Dimensional Electron and Hole Systems* (Springer, 2003).
32. Pryor, C., Kim, J., Wang, L. W., Williamson, A. J. & Zunger, A. Comparison of two methods for describing the strain profiles in quantum dots. *J. Appl. Phys.* **83**, 2548 (1998).
33. Bester, G., Zunger, A., Wu, X. & Vanderbilt, D. Effects of linear and nonlinear piezoelectricity on the electronic properties of InAs/GaAs quantum dots. *Phys. Rev. B* **74**, 081305(R) (2006).
34. Bester, G., Wu, X., Vanderbilt, D. & Zunger, A. Importance of second-order piezoelectric effects in zinc-blende semiconductors. *Phys. Rev. Lett.* **96**, 187602 (2006).
35. Caro, M. A., Schulz, S. & O'Reilly, E. P. Origin of nonlinear piezoelectricity in III-V semiconductors: Internal strain and bond ionicity from hybrid-functional density functional theory. *Phys. Rev. B* **91**, 075203 (2015).
36. Gawarecki, K. Spin-orbit coupling and magnetic-field dependence of carrier states in a self-assembled quantum dot. *Phys. Rev. B* **97**, 235408 (2018).
37. Krzykowski, M., Gawarecki, K. & Machnikowski, P. Hole spin-flip transitions in a self-assembled quantum dot. *Phys. Rev. B* **102**, 205301 (2020).
38. Świdorski, M. & Zieliński, M. Exact Diagonalization Approach for Atomistic Calculation of Piezoelectric Effects in Semiconductor Quantum Dots. *Acta Phys. Pol. A* **129**, 79–82 (2016).
39. Azizi, M. & Machnikowski, P. Interband Coulomb coupling in narrow-gap semiconductor nanocrystals: $\mathbf{k}\cdot\mathbf{p}$ theory. *Phys. Rev. B* **91**, 195314 (2015).
40. Karwat, P., Gawarecki, K. & Machnikowski, P. Phonon-assisted carrier tunneling with hyperfine-induced spin flip in coupled quantum dot systems. *Phys. Rev. B* **104**, 045308 (2021).

41. Gawęlczyk, M. *et al.* Exciton lifetime and emission polarization dispersion in strongly in-plane asymmetric nanostructures. *Phys. Rev. B* **96**, 245425 (2017).
42. Shah, J. *Ultrafast spectroscopy of semiconductors and semiconductor nanostructures* (Springer Science & Business Media, 2013).
43. Wigger, D. *et al.* Rabi oscillations of a quantum dot exciton coupled to acoustic phonons: coherence and population readout. *Optica* **5**, 1442–1450 (2018).
44. Hahn, T., Kasprzak, J., Machnikowski, P., Kuhn, T. & Wigger, D. Influence of local fields on the dynamics of four-wave mixing signals from 2D semiconductor systems. *New J. Phys.* **23**, 023036 (2021).
45. Hahn, T. *et al.* Destructive photon echo formation in six-wave mixing signals of a MoSe₂ monolayer. *Adv. Sci.* **9**, 2103813 (2022).
46. Kasprzak, J. *et al.* Coherent dynamics of a single Mn-doped quantum dot revealed by four-wave mixing spectroscopy. *ACS Photonics* **9**, 1033–1041 (2022).
47. Wigger, D. *et al.* Acoustic phonon sideband dynamics during polaron formation in a single quantum dot. *Opt. Lett.* **45**, 919–922 (2020).
48. Wigger, D. *et al.* Exploring coherence of individual excitons in InAs quantum dots embedded in natural photonic defects: influence of the excitation intensity. *Phys. Rev. B* **96**, 165311 (2017).
49. Bopp, F. *et al.* Quantum dot molecule devices with optical control of charge status and electronic control of coupling. *Adv. Quantum Technol.* **5**, 2200049 (2022).
50. Kim, D., Carter, S. G., Greilich, A., Bracker, A. S. & Gammon, D. Ultrafast optical control of entanglement between two quantum-dot spins. *Nat. Phys.* **7**, 223–229 (2011).
51. Greilich, A., Carter, S. G., Kim, D., Bracker, A. S. & Gammon, D. Optical control of one and two hole spins in interacting quantum dots. *Nat. Photonics* **5**, 702–708 (2011).
52. Weiss, K. M., Elzerman, J. M., Delley, Y. L., Miguel-Sanchez, J. & Imamoglu, A. Coherent two-electron spin qubits in an optically active pair of coupled InGaAs quantum dots. *Phys. Rev. Lett.* **109**, 107401 (2012).

Controlled Coherent Coupling in a Quantum Dot Molecule Revealed by Ultrafast Four-Wave Mixing Spectroscopy (Supporting Information)

Daniel Wigger,^{1,2,*} Johannes Schall,³ Marielle Deconinck,³ Nikolai Bart,⁴ Paweł Mrowiński,^{1,5} Mateusz Krzykowski,¹ Krzysztof Gawarecki,¹ Martin von Helversen,³ Ronny Schmidt,³ Lucas Bremer,³ Frederik Bopp,⁶ Dirk Reuter,⁷ Andreas D. Wieck,⁴ Sven Rodt,³ Julien Renard,⁸ Gilles Nogues,⁸ Arne Ludwig,⁴ Paweł Machnikowski,¹ Jonathan J. Finley,⁶ Stephan Reitzenstein,³ Jacek Kasprzak^{6,8,*}

¹*Institute of Theoretical Physics, Wrocław University of Science and Technology, 50-370 Wrocław, Poland*

²*School of Physics, Trinity College Dublin, Dublin 2, D02 PN40, Ireland*

³*Institute of Solid State Physics, Technische Universität Berlin, 10623 Berlin, Germany*

⁴*Lehrstuhl für Angewandte Festkörperphysik Ruhr-Universität Bochum, 44780 Bochum, Germany*

⁵*Laboratory for Optical Spectroscopy of Nanostructures, Department of Experimental Physics, Wrocław University of Technology, 50-370 Wrocław, Poland*

⁶*Walter Schottky Institut and Physik Department, Technische Universität München, 85748 Garching, Germany*

⁷*Department Physik, Universität Paderborn, 33098 Paderborn, Germany*

⁸*Université Grenoble Alpes, CNRS, Grenoble INP, Institut Néel, 38000 Grenoble, France*

**daniel.wigger@tcd.ie, jacek.kasprzak@neel.cnrs.fr*

This document contains:

S1. Four-wave mixing experiment

- S1A. Experimental method and device**
- S1B. Coherence dynamics**
- S1C. Rabi rotations**
- S1D. Identification of the neutral exciton-biexciton complex**
- S1E. Power dependence of PL spectra**
- S1F. Fitting 2D FWM spectra**

S2. Theory

- S2A. Semi-empirical model**
- S2B. Calculation of 2D spectra for ultra-short pulses**
- S2C. Dynamical simulations**
- S2D. Inhomogeneous dephasing**
- S2E. $k \cdot p$ model**

S1. Four-wave mixing experiment

In this section we present details on the performed experiment and used sample (Sec. S1A). We show standard characterization measurements of the coherence (Sec. S1B) and light-matter coupling (Sec. S1C). Further, we identify the neutral exciton transition (Sec. S1D), demonstrate the power dependence of the photoluminescence (PL) spectra (Sec. S2E), and describe our fitting procedure for the 2D spectra (Sec. S1F).

S1A. Experimental method and device

We employ the heterodyne spectral interferometry technique introduced in Ref. [1] to detect four-wave mixing (FWM) signals from the quantum dot molecule (QDM). Its two-beam version was described in detail in the Supplementary Material of Ref. [2], while its extension to a three-beams configuration was presented in the Supplementary Material of Ref. [3]. We use a Ti:Sapphire femto-second oscillator tuned into resonance with bright excitonic (trion) transitions of the QDM around 930 nm (1333 meV). In order to avoid driving spectrally nearby transitions, for instance biexcitons, the pulses are spectrally shaped (with a passive, diffraction grating-based pulse shaper) increasing their duration to ≈ 0.4 ps (full width at half maximum of the intensity spectrum). The main beam is then split into the reference pulse \mathcal{E}_R and three excitation pulses $\mathcal{E}_{1,2,3}$. In the latter, the consecutive pulses in the train are distinctly phase-shifted using acousto-optic modulators driven at the radio-frequencies $(\Omega_1, \Omega_2, \Omega_3) = (80, 79, 79.77)$ MHz. Using mechanical delay stages, they then acquire respective delays τ_{12} and τ_{23} , between the first two and last two arriving beams, respectively. $\mathcal{E}_{1,2,3}$ are recombined into the same spatial mode and propagate unidirectionally. Using an external microscope objective, $\mathcal{E}_{1,2,3}$ are focused on the sample surface, impinging the central part of the circular Bragg grating, while \mathcal{E}_R is placed on the flat surface around 15 μm apart (Fig. S1). The signal is collected in the reflection direction. The reflection from the QDM, which also contains the FWM signal, is interfered with \mathcal{E}_R and heterodyned at the frequency $\Omega_3 + \Omega_1 - \Omega_1$ in the same manner as explained in previous publications [1, 2, 3, 4]. Note, that in this work we apply the degenerate two-pulse FWM scheme, i.e., $\tau_{23} = 0$.

The sample is kept in a He-flow cold-finger cryostat at the temperature of 7 K. To tune the spectral separation between quantum

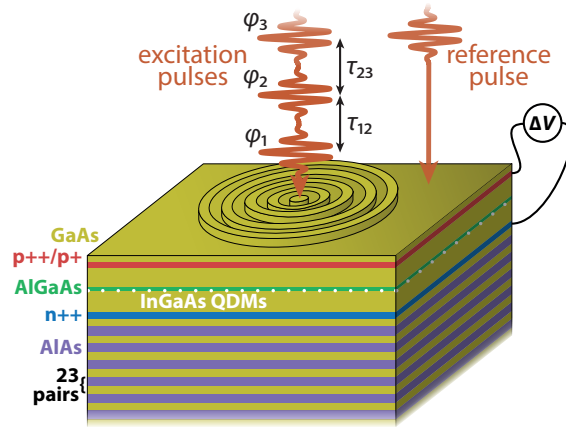


Figure S1: Schematic picture of the sample structure. Above a GaAs/AlAs distributed Bragg structure the InGaAs quantum dot molecule (QDM) layer is sandwiched between charge-doped layers, which are connected to a bias source. For details on the sample design and processing we refer to Ref. [5]. The optical in- and out-coupling is improved by a circular Bragg grating, also called a bulls-eye photonic structure, on the top surface. The laser pulses used for the optical excitation in the four-wave mixing experiment are focused on the center of the grating, while the reference beam hits the free surface in the vicinity.

levels in the QDM, we vary the gate voltage ΔV (Fig. S1), supplied by an external voltage source micro-bonded to the electrodes of the QDM device via the feed-through connectors of the cryostat. In the initial part of the experiment, the current-voltage characterization was carried out (not shown). To assure a safe operation of the p-i-n diode the current is limited to 80 μA . The voltage source, provided by *Keithley*, is interfaced via the General Purpose Interface Bus (GPIB) with the home-developed software controlling the whole experiment.

S1B. Coherence dynamics

Figure S2 shows an exemplary coherence dynamics measurement by varying the delay τ_{12} in the FWM experiment. While the neutral exciton line only decays due to dephasing processes, the trion transitions exhibit pronounced oscillations. These involved dynamics originate from the coherent coupling between the different states and lead to the off-diagonal peaks in the 2D FWM spectra (see e.g. Fig. S7).

The beat dynamics in the FWM signal is suppressed when only one of the transitions is optically driven. For such a measurement

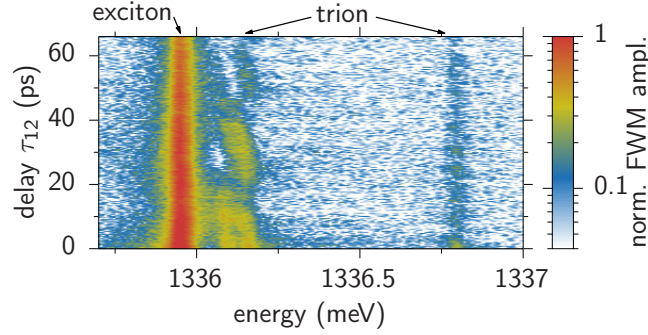


Figure S2: Spectral dynamics of the trion transitions as a function of the delay τ_{12} . The trion lines show a coherence beating due to the coherent coupling. The exciton line just decays due to the decoherence of the zero phonon line.

the spectrally integrated FWM amplitude of the neutral exciton is shown in Fig. S3. By fitting the long-time decay with a single exponential function, we deduce a dephasing time of 200 ps. This dephasing rate is used for the simulations in Fig. S10. The initial rapid drop of the FWM amplitude is most likely stemming from a phonon-induced dephasing process [6] and is not further investigated here.

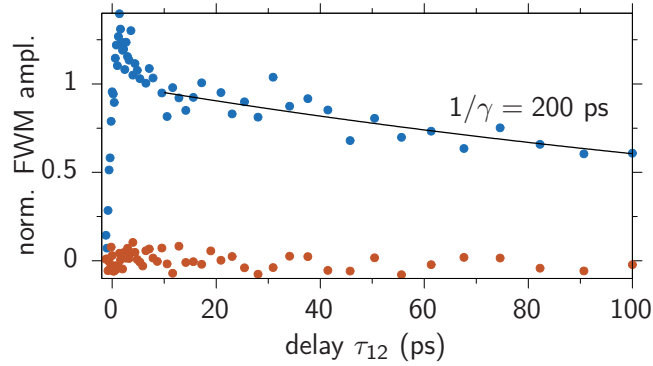


Figure S3: Spectrally integrated coherence dynamics as a function of τ_{12} of the neutral exciton line, measured far from the hole tunneling resonance (blue points). The orange points represent the noise level. The long-time decay is fitted with a single exponential with the dephasing time 200 ps. The initial faster decay is due to phonon-induced dephasing.

S1C. Rabi rotations

To characterize the strength of the light-matter coupling of the QDM in Fig. S4 we plot the spectrally integrated FWM amplitude (for $\tau_{12} = 0$) as a function of the applied laser pulse amplitude. We find the expected Rabi rotation behavior [7], which shows that a pulse area of $\pi/2$ is found for a pulse amplitude around $\sqrt{P_1} = 0.7 \sqrt{\mu\text{W}}$. For all measurement in this work we restrict ourselves to small excitation powers in the linear regime of the Rabi rotation, i.e., $\sqrt{P_1} < 0.05 \sqrt{\mu\text{W}}$.

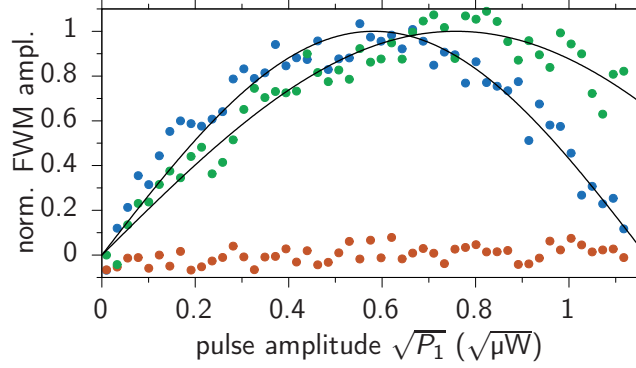


Figure S4: Rabi rotation experiment, performed on the neutral exciton (blue points) and the trion (green points) transitions. The orange points represent the noise level. Pulse areas of $\pi/2$ are found for pulse amplitudes around $0.7 \sqrt{\mu\text{W}}$.

S1D. Identification of the neutral exciton-biexciton complex

As stated in the main text, the bright spectral line in Fig. 3(a) stems from a neutral exciton transition. The standard proof of this type of transition is the detection of a coupled biexciton state [2]. We do this through the 2D FWM spectrum in Fig. S5, where the biexciton appears as off-diagonal peak with a binding energy of around 2.8 meV, which is a typical value for InGaAs QDs [8].

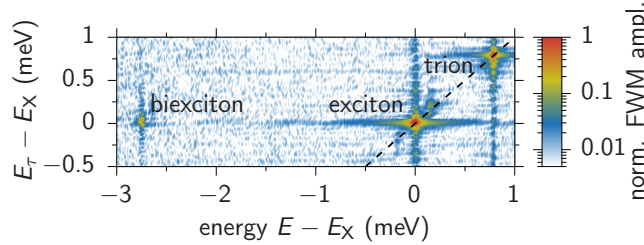


Figure S5: 2D FWM spectrum showing the exciton-biexciton transition as off-diagonal peak. The exciton and trion transitions appear on the diagonal.

S1E. Power dependence of PL spectra

We have seen in the main text, that the bias ranges where the hole and trion resonances appear differ between the presented PL and FWM measurements. In Fig. S6(a) we show the same data as in Fig. 1(a) in the main text for an optical excitation power of $P = 100 \text{ nW}$ and in (b) the same measurement for $P = 400 \text{ nW}$. We find the same spectral features of line-shifts and avoided-crossings but on different bias intervals. The range is not only shifted but also scaled by almost a factor of 2. This shows that the bias-dependence of the different state energies strongly depends on the specific optical excitation conditions. We also note that even more different scenarios are observed upon additional white light illumination (not shown). Varying optical excitation, changes the free carrier density and thus also the energetic level structure in the p-i-n diode and also the alignment of the quantized levels in the QDM itself. Therefore, because already the general optical excitation schemes in PL and FWM are off-resonant and resonant, respectively, and consequently entirely different, the two experiments cannot be quantitatively compared regarding their bias range properly.

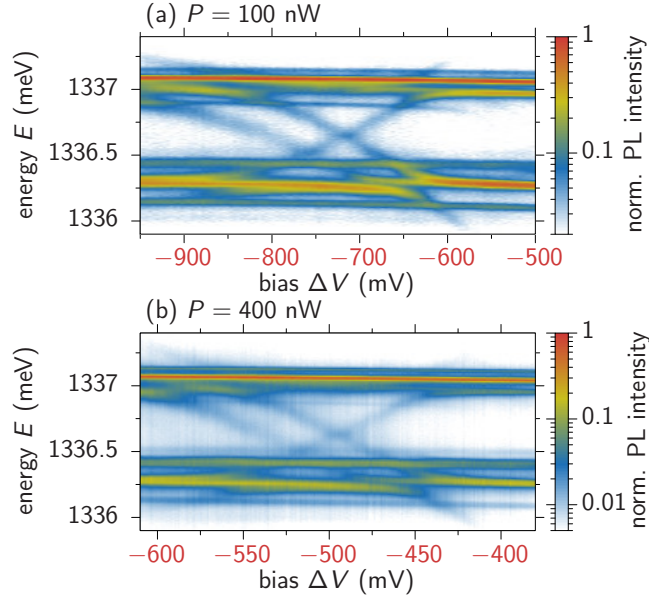


Figure S6: Bias scans of the PL intensity for two different excitation powers. (a) Same as Fig. 1(a) in the main text with $P = 100$ nW. (b) 400 nW depicted for a different bias range than (a).

S1F. Fitting 2D FWM spectra

To efficiently remove the prominent impact of the neutral exciton transition from the 2D spectra depicted in Fig. S7 we fit each spectrum with a sum of 2D Lorentzians. While for most studied bias values we use one diagonal peak for the exciton and two diagonal and two off-diagonal ones for the trion transitions, for the bias values $\Delta V = -307$, -312 , and -320 mV we have to consider one additional diagonal and two additional off-diagonal peaks. This appearance of additional peaks in the bias range directly reflects the development of an avoided-crossing in the linear spectra (see Fig. 3(a) in the main text).

Our goal is to determine the peak ratio in the 2D spectra consistently in the measured and the simulated data. Therefore, we simply focus on four parts marked by colored areas (dashed squares) in Fig. S7(o). The signal amplitude summed over the red shaded areas gives the diagonal contributions and the sum over the green shaded areas the off-diagonal ones. This procedure can be easily automated to retrieve the peak ratios (green areas/red areas) for many bias values in the simulation, i.e., many 2D spectra. To determine the experimental peak ratios we use the fitted 2D spectra to reduce the uncertainties stemming from different discretization or spectral oscillations due to insufficiently long delay ranges.

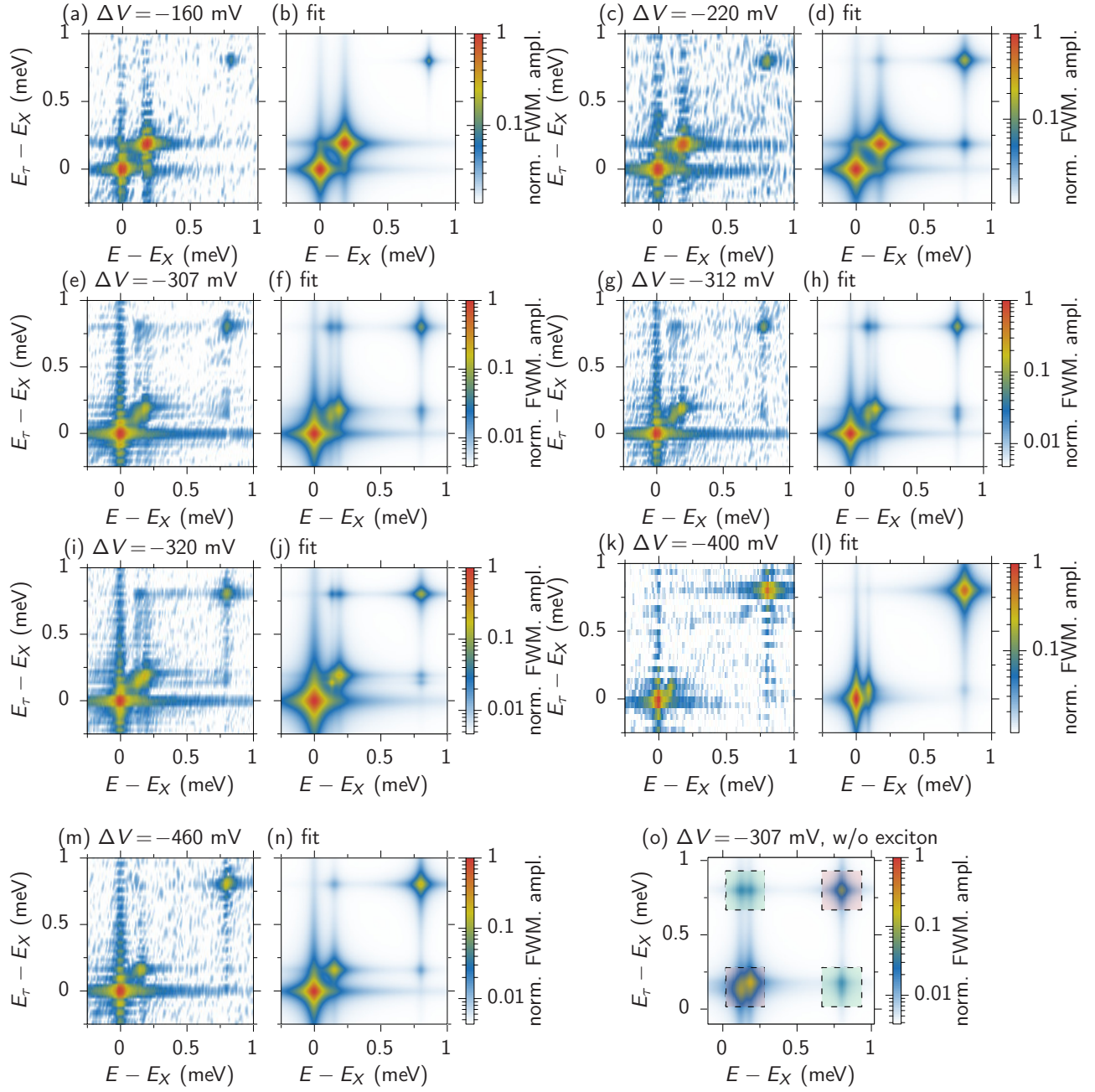


Figure S7: (a)-(n) Measured 2D FWM spectra with respective fits for different bias values. The fit function is a sum of 2D Lorentzians. (o) Fitted 2D FWM spectrum for $\Delta V = -307$ mV without the neutral exciton line. The red shaded areas mark the integration range for the diagonal contributions, the green areas those for the off-diagonal ones.

S2. Theory

Here, we present the details of the semi-empirical theory for the coupled hole and trion system (Sec. S2A). This model yields transition energies and amplitudes for dipole-allowed transitions that are used for determining the FWM spectrum from the analytical formulas in the ultra-short pulse limit (Sec. S2B) or from dynamical simulations (Sec. S2C). Further, we discuss the influence of an inhomogeneous dephasing on the 2D spectra (Sec. S2D). Finally, we present the $\mathbf{k} \cdot \mathbf{p}$ model and the spectra calculated from the system's eigenstates and eigenenergies obtained in this way (Sec. S2E).

S2A. Semi-empirical model

In the following electron and hole destruction (creation) operators are given by $a_{\sigma}^{(\dagger)}$ and $h_{n,\sigma}^{(\dagger)}$ for the spin orientation $\sigma \in \{\uparrow, \downarrow\}$, respectively, and $n \in \{1, 2\}$ indicates in which QD the hole is located.

The relevant single particle states of the QDM are given by the single hole states forming the ground states, which are charac-

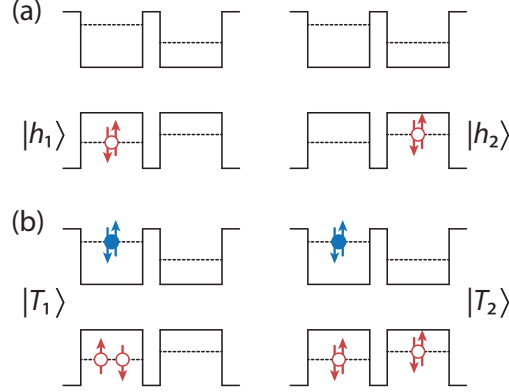


Figure S8: Schematic picture illustrating the different (a) hole and (b) trion states in the QDM taking into account the spins of the particles.

terized by the QD number and the spin orientation: $|1_{\uparrow}\rangle, |1_{\downarrow}\rangle, |2_{\uparrow}\rangle, |2_{\downarrow}\rangle$. The relevant trions forming the excited states emerge by the creation of an additional electron-hole pair, with the electron always in QD1. These three-particle complexes now possess two holes, whose spin coupling results in new eigenstates that can be sorted into singlet $|S_{(m,n)}\rangle$ ($m, n \in \{1, 2\}$) and triplet states $|T_{\alpha}\rangle$ ($\alpha \in \{+, -, 0\}$) defined by

$$|S_{(2,0)}\rangle = h_{1,\uparrow}^{\dagger} h_{1,\downarrow}^{\dagger} |0\rangle \quad (\text{S1a})$$

$$|S_{(1,1)}\rangle = \frac{1}{\sqrt{2}} (h_{1,\uparrow}^{\dagger} h_{2,\downarrow}^{\dagger} - h_{1,\downarrow}^{\dagger} h_{2,\uparrow}^{\dagger}) |0\rangle \quad (\text{S1b})$$

$$|S_{(0,2)}\rangle = h_{2,\uparrow}^{\dagger} h_{2,\downarrow}^{\dagger} |0\rangle \quad (\text{S1c})$$

$$|T_{+}\rangle = h_{1,\uparrow}^{\dagger} h_{2,\uparrow}^{\dagger} |0\rangle \quad (\text{S1d})$$

$$|T_{-}\rangle = h_{1,\downarrow}^{\dagger} h_{2,\downarrow}^{\dagger} |0\rangle \quad (\text{S1e})$$

$$|T_0\rangle = \frac{1}{\sqrt{2}} (h_{1,\uparrow}^{\dagger} h_{2,\downarrow}^{\dagger} + h_{1,\downarrow}^{\dagger} h_{2,\uparrow}^{\dagger}) |0\rangle \quad (\text{S1f})$$

To get the full trion wave function we have to add the spin orientation $\sigma \in \{\uparrow, \downarrow\}$ of the remaining electron to the states such that we get $|\sigma, S_{(m,n)}\rangle$ and $|\sigma, T_{\alpha}\rangle$. Overall we have 4 ground/hole states and 12 excited/trion states.

For the minimal model introduced in the main text we may identify $|h_1\rangle \rightarrow |1_{\uparrow}\rangle$, $|h_2\rangle \rightarrow |2_{\uparrow}\rangle$, $|T_1\rangle \rightarrow |S_{2,0}\rangle$, and $|T_2\rangle \rightarrow |S_{1,1}\rangle$ (see Fig. S8).

The ground/hole state Hamiltonian reads:

$$H_{h,\sigma} = \sum_{\sigma=\uparrow,\downarrow} [(V_2 - F) |2_{\sigma}\rangle \langle 2_{\sigma}| + t (|1_{\sigma}\rangle \langle 2_{\sigma}| + \text{h.c.})], \quad (\text{S2})$$

where V_2 is the energy difference between the ground states in the two QDs, $F = ed\mathcal{E}_z$ is the dipole energy associated with the charge displacement in the axial electric field \mathcal{E}_z , where d is the effective distance between the QDs and e is the elementary charge, and t is the tunnel coupling.

The excited/trion state Hamiltonian reads (dropping the conserved electron spin index σ on the right-hand side):

$$\begin{aligned}
H_{T,\sigma} = & J \left(|S_{(1,1)}\rangle \langle S_{(1,1)}| - \sum_{+, -, 0} |T_\alpha\rangle \langle T_\alpha| \right) \\
& + 2V_c |S_{(0,2)}\rangle \langle S_{(0,2)}| \\
& + \sum_{m,n=1,2} n (V'_2 - F) |S_{(m,n)}\rangle \langle S_{(m,n)}| \\
& + \sum_{\alpha=+, -, 0} (V'_2 - F) |T_\alpha\rangle \langle T_\alpha| \\
& + t (|S_{(1,1)}\rangle \langle S_{(0,2)}| + |S_{(1,1)}\rangle \langle S_{(0,2)}| + \text{h.c.}) .
\end{aligned} \tag{S3}$$

Here, J is the hole exchange splitting, V_c is the Coulomb energy of exciton dissociation, and V'_2 is the hole energy difference between the QDs in the presence of the exciton (taking the Coulomb correlation energy into account). The total trion Hamiltonian is

$$H_T = H_{T,\uparrow} + H_{T,\downarrow} \tag{S4}$$

The Hamiltonian for the electron-hole short-range exchange interaction is most conveniently written in the second quantization form, reading

$$H^{\text{ex}} = \delta \left(a_{\uparrow}^\dagger h_{\downarrow}^\dagger h_{\downarrow} a_{\uparrow} + a_{\downarrow}^\dagger h_{\uparrow}^\dagger h_{\uparrow} a_{\downarrow} \right). \tag{S5}$$

The considered values of the system parameters are $V_c = 20$ meV, $V_2 = 0$ (this parameter merely sets the reference for the electric field; with this choice the $F = 0$ is fixed at the hole resonance), $V'_2 = 0.785$ meV, $\delta = 0.21$ meV, $J = 0$. With these parameters, the model is equivalent to the one used in Ref. [5].

The dipole operators for σ_+ and σ_- polarized light are, respectively,

$$M^{(+)} = h_{1\uparrow} a_{\downarrow} = |1_{\downarrow}\rangle \langle \downarrow, S_{(2,0)}| + |2_{\downarrow}\rangle \left(\frac{1}{\sqrt{2}} \langle \downarrow, S_{(1,1)}| + \langle \downarrow, T_-| + \frac{1}{\sqrt{2}} \langle \downarrow, T_0| \right), \tag{S6}$$

and

$$M^{(-)} = h_{1\downarrow} a_{\uparrow} = |1_{\uparrow}\rangle \langle \uparrow, S_{(2,0)}| + |2_{\uparrow}\rangle \left(\frac{1}{\sqrt{2}} \langle \uparrow, S_{(1,1)}| + \langle \uparrow, T_+| + \frac{1}{\sqrt{2}} \langle \uparrow, T_0| \right), \tag{S7}$$

which determines the optically active transitions in the system.

S2B. Calculation of 2D spectra for ultra-short pulses

Using the matrix of transition amplitudes between the hole and trion states M_{iu} , we can derive the two-pulse FWM spectrum in a general analytical way in the limit of ultra-short laser pulses.

The diagonalized Hamiltonian is of the form

$$H = \sum_i E_i |\mathfrak{h}_i\rangle \langle \mathfrak{h}_i| + \sum_u E_u |\mathfrak{T}_u\rangle \langle \mathfrak{T}_u| + [\mathcal{E}(t + \tau_{12}) e^{i\varphi_1} + \mathcal{E}(t) e^{i\varphi_2} + \text{h.c.}] M, \tag{S8}$$

where $|\mathfrak{h}_i\rangle$ and $|\mathfrak{T}_j\rangle$ are the hole and electron eigenstates, respectively, with the corresponding eigenenergies E_i and E_u ,

$$\mathcal{E}(t) = \hat{\mathcal{E}}(t) e^{-i\omega t},$$

and M is one of the operators in Eq. (S6) or Eq. (S7), depending on the polarization of light. In the interaction picture this reads

$$\tilde{H}(t) = [\mathcal{E}(t + \tau_{12}) e^{i\varphi_1} + 2\mathcal{E}(t) e^{i(\varphi_2 + \varphi_3)} + \text{h.c.}] \tilde{M}(t),$$

where

$$\tilde{M}(t) = \sum_{i,u} M_{iu} |\mathfrak{T}_u\rangle \langle \mathfrak{h}_i| e^{i\omega_{iu} t},$$

with $\omega_{iu} = (E_u - E_i)/\hbar$.

Before any optical excitation the system state is a mixture of hole states represented by a density matrix $\rho^{(0)}$. The first optical excitation happens at $t = -\tau_{12}$ and we assume that the laser pulse is much faster than any internal dynamics, i.e., dephasing, tunneling, or decay. The density matrix immediately after this pulse is then given by

$$\begin{aligned}\rho^{(1)} &= -\frac{i}{\hbar} \int_{-\tau_{12}-\varepsilon}^{-\tau_{12}+\varepsilon} [\tilde{H}(t), \rho^{(0)}] dt \\ &= -\frac{i}{\hbar} \int_{-\infty}^{\infty} \hat{\mathcal{E}}^*(t + \tau_{12}) e^{-i\varphi_1} \rho^{(0)} \sum_{i,u} M_{iu}^* |\mathfrak{h}_i\rangle \langle \mathfrak{T}_u| e^{-i\omega_{iu}t} e^{-i\omega(t+\tau_{12})} dt + \text{h.c.},\end{aligned}\quad (\text{S9})$$

where h.c. contains the phase $+\varphi_1$, which is irrelevant for the final FWM signal and can therefore directly be neglected. After introducing the pulse spectrum,

$$\hat{s}(\omega) = \int_{-\infty}^{\infty} \hat{\mathcal{E}}(t) e^{-i\omega t} dt, \quad (\text{S10})$$

the FWM-relevant density matrix after the first pulse reads

$$\rho^{(1)}(\tau_{12}) = -\frac{i}{\hbar} e^{-i\varphi_1} \rho^{(0)} e^{i\omega_{iu}\tau_{12}} \sum_{i,u} M_{iu}^* |\mathfrak{h}_i\rangle \langle \mathfrak{T}_u| \hat{s}^*(\omega - \omega_{iu}) = \sum_{iu} \rho_{iu}^{(1)} |\mathfrak{h}_i\rangle \langle \mathfrak{T}_u|. \quad (\text{S11})$$

Before the interaction with the second pulse, the system can undergo dephasing and decay dynamics, such that the density matrix immediately before the next pulse is given by

$$\rho^{(1)}(0 - \varepsilon) = \sum_{i,u} \rho_{iu}^{(1)}(\tau_{12}, \omega) |\mathfrak{h}_i\rangle \langle \mathfrak{T}_u| e^{-\gamma_{iu}\tau_{12}}, \quad (\text{S12})$$

where γ_{iu} is the dephasing rate for a given coherence.

The second pulse acts via a second order process, which leads to the density matrix

$$\begin{aligned}\rho^{(2)} &= -\frac{1}{\hbar^2} \int_{-\varepsilon}^{\varepsilon} \int_{-\varepsilon}^t [\tilde{H}(t), [\tilde{H}(t'), \rho^{(1)}]] dt' dt \\ &= \frac{1}{\hbar^2} \int_{-\varepsilon}^{\varepsilon} \int_{-\varepsilon}^{\varepsilon} \tilde{H}(t) \rho^{(1)} \tilde{H}(t') dt' dt.\end{aligned}\quad (\text{S13})$$

When considering again only contributions with the correct phase dependence for the FWM signal ($\sim e^{2i\varphi_2}$) we arrive at

$$\begin{aligned}\rho^{(2)} &= \frac{1}{\hbar^2} e^{i2\varphi_2} \int_{-\infty}^{\infty} \hat{\mathcal{E}}(t) e^{-i\omega t} \sum_{j,v} M_{jv} |\mathfrak{T}_v\rangle \langle \mathfrak{h}_j| e^{i\omega_{jv}t} \rho^{(1)} \int_{-\infty}^{\infty} \hat{\mathcal{E}}(t) e^{-i\omega t} \sum_{k,w} M_{kw} |\mathfrak{T}_w\rangle \langle \mathfrak{h}_k| e^{i\omega_{kw}t} \\ &= \frac{1}{\hbar^2} e^{2i\varphi_2} \sum_{j,k,v,w} \hat{s}(\omega - \omega_{jv}) \hat{s}(\omega - \omega_{kw}) M_{jv} M_{kw} |\mathfrak{T}_v\rangle \langle \mathfrak{h}_j| \rho^{(1)} |\mathfrak{T}_w\rangle \langle \mathfrak{h}_k| \\ &= -\frac{i}{\hbar^2} e^{i(2\varphi_2 - \varphi_1)} \sum_{i,j,k,u,v,w} \hat{s}^*(\omega - \omega_{iu}) \hat{s}(\omega - \omega_{jv}) \hat{s}(\omega - \omega_{kw}) \\ &\quad \times M_{iu}^* M_{jv} M_{kw} e^{(i\omega_{iu} - \gamma_{iu})\tau_{12}} |\mathfrak{T}_v\rangle \langle \mathfrak{h}_j| \rho^{(0)} |\mathfrak{h}_i\rangle \langle \mathfrak{T}_u| |\mathfrak{T}_w\rangle \langle \mathfrak{h}_k|.\end{aligned}\quad (\text{S14})$$

Finally, taking into account that the emission resulting from a coherence $|\mathfrak{T}_v\rangle \langle \mathfrak{h}_k|$ is proportional to $M_{kv}^* e^{(-i\omega_{kv} - \gamma_{kv})t}$, we arrive at the FWM signal

$$\rho^{(\text{FWM})} \sim \sum_{i,j,k,u,v} \hat{s}^*(\omega - \omega_{iu}) \hat{s}(\omega - \omega_{jv}) \hat{s}(\omega - \omega_{ku}) \rho_{ij}^{(0)} M_{iu}^* M_{jv} M_{ku} M_{kv}^* e^{(-i\omega_{kv} - \gamma_{kv})t} e^{(i\omega_{iu} - \gamma_{iu})\tau_{12}}. \quad (\text{S15})$$

Assuming that the spectrum of the laser pulses is much broader than the energy differences between the relevant transitions, we can set $\hat{s}(\omega - \omega_{mn}) \approx 1$. We further assume that the initial state is a statistical mixture of the hole states, i.e.,

$$\rho^{(0)} = \sum_n p_n |\mathfrak{h}_n\rangle \langle \mathfrak{h}_n|,$$

where we take the thermal distribution for the probabilities p_n . With this the FWM signal can be simplified to

$$\rho^{(\text{FWM})}(t, \tau_{12}) \sim \sum_n p_n \sum_{k,u,v} M_{nu}^* M_{nv} M_{ku} M_{kv}^* e^{(-i\omega_{kv} - \gamma_{kv})t} e^{(i\omega_{nu} - \gamma_{nu})\tau_{12}}. \quad (\text{S16})$$

From this we directly find the 2D FWM spectrum

$$\rho^{(\text{FWM})}(\omega, \omega_\tau) \sim \sum_n p_n \sum_{k,u,v} f_{nu}(\omega_\tau - \omega_{nu}) f_{kv}^*(\omega - \omega_{kv}) M_{nu}^* M_{nv} M_{ku} M_{kv}^*, \quad (\text{S17})$$

where $f_{iu}(\omega)$ is broadened by γ_{iu} but also takes the spectral broadening by a finite spectral resolution in the detection process into account.

A few examples for the analytically calculated 2D spectra are shown in Fig. S9 for different bias values as given in the plot. We

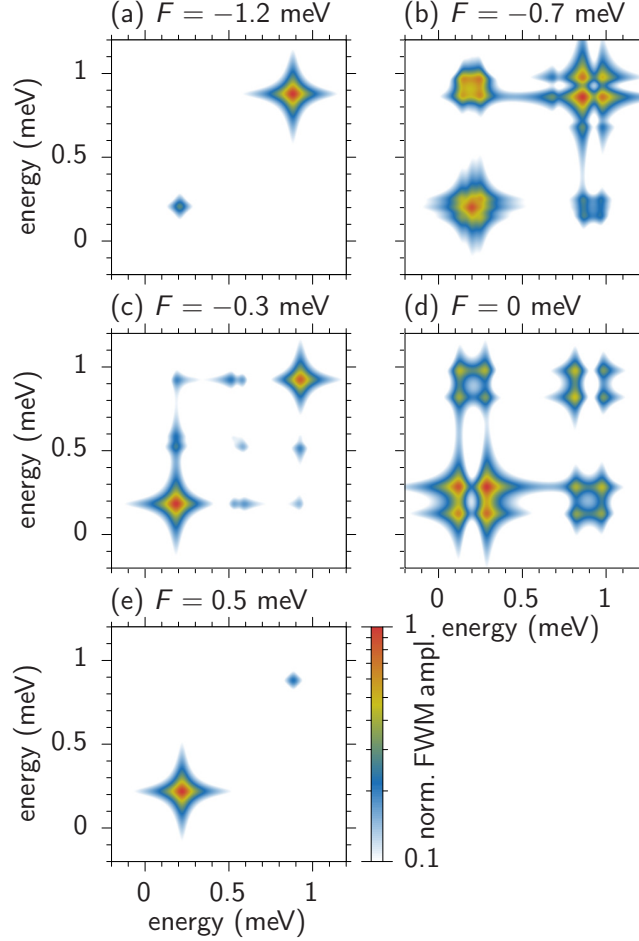


Figure S9: Simulated 2D FWM spectrum using Eq. (S17) for different external electric fields as labeled in each panel.

assume that the spectral broadening is dominated by the instrumental resolution and use the same value as in Fig. 2 in the main text, which roughly agrees with the spectrometer resolution in the experiment. We clearly see that the off-diagonal peaks only appear when the states are efficiently tunnel-coupled in the vicinity of the avoided-crossings in the bias scan (Fig. 2 or S10).

S2C. Dynamical simulations

To simulate the FWM signal while taking a non-vanishing pulse duration into account we calculate the system's dynamics by solving the Lindblad equation for several combinations of pulse phases $e^{i\varphi_1}$ and $e^{i\varphi_2}$ [9, 10]. We then phase-filter the optically active coherences p in the density matrix by numerically integrating $\int_{\varphi_1, \varphi_2} p e^{-i(2\varphi_2 - \varphi_1)} d\varphi_1 d\varphi_2$. For a given pulse delay τ_{12} we then determine the FWM spectrum by Fourier transforming the filtered coherence with respect to the real time t after the last

arriving laser pulse. The bias scan of the FWM spectrum calculated dynamically is depicted in Fig. S10. We consider a pulse duration (Gaussian standard deviation of the electric field) of 200 fs (this roughly agrees with the full width at half maximum duration of the pulse intensity of 400 fs), a pulse delay of 1 ps, and the previously determined dephasing time of 200 ps. The spectral lines are additionally broadened according to the spectral resolution of the experiment. The most important features, like the pattern of avoided-crossings and intensity distributions agree well with the analytic simulation depicted in Fig. 2 in the main text for a vanishing pulse duration. This shows that the assumption of a flat laser pulse spectrum is a valid approximation to calculate the FWM response.

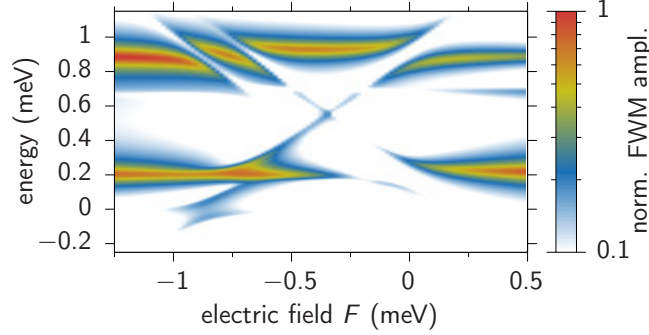


Figure S10: Theoretical bias scan of the FWM spectrum by solving the Lindblad equation and taking into account a non-vanishing pulse duration of 200 fs.

S2D. Inhomogeneous dephasing

In general, inhomogeneous dephasing of a single emitter system originates from fluctuations of the transition energy which happens on timescales slower than a single repetition of the FWM experiment but faster than the repetition rate of the laser. Formally, this situation corresponds to an ensemble measurement. In order to include such slow fluctuations, we assume the transition frequencies ω_{kv}, ω_{nu} in Eq. (S16) to be Gaussian random variables with mean values $\bar{\omega}_{kv}, \bar{\omega}_{nu}$ and standard deviation σ , which are uncorrelated if $k \neq n$ or $v \neq u$. Upon averaging over the fluctuations, we arrive at

$$\rho^{(\text{FWM})}(t, \tau_{12}) \sim \sum_n p_n \sum_{k,u,v} M_{nu}^* M_{nv} M_{ku} M_{kv}^* \times e^{(-i\bar{\omega}_{kv} - \gamma_{kv})t} e^{(i\bar{\omega}_{nu} - \gamma_{nu})\tau_{12}} f_{\text{deph}}(t, \tau_{12}).$$

where the dephasing factor is

$$f_{\text{deph}}(t, \tau_{12}) = \begin{cases} e^{-\sigma^2(t^2 + \tau_{12}^2)}, & k \neq n \text{ or } v \neq u, \\ e^{-\sigma^2(t - \tau_{12})^2}, & k = n \text{ and } v = u. \end{cases}$$

The impact of the inhomogeneous dephasing is shown in Fig. S11, where we show the 2D FWM spectrum without inhomogeneous broadening, i.e., $\sigma = 0$ [$F = 0$, same as Fig. S9(d)] in (a) and $\sigma = 0.1$ meV in (b). When presenting the results, we subtract the “background” formed by the power-law tails of the strong diagonal peaks in the spectral area of the off-diagonal ones. We clearly see that the previously sharp peaks get additionally broadened predominantly into the diagonal direction in the 2D spectrum, as well known from several previous works [11]. In Fig. S11(c) we show peak ratios of the form $\sum A_{\text{off-diag}} / \sum A_{\text{diag}}$ as in the main text and increase the inhomogeneous broadening as given in the plot. The values of $A_{\text{off-diag}}$ and A_{diag} are determined by integrating the simulated signal over the areas shown in Fig. S7(o), with $A_{\text{off-diag}}$ representing the difference of the counting results for the full signal and for the signal with off-diagonal contributions artificially switched off (when only the tails of the strong diagonal peaks contribute). As discussed in the main text, the additional dephasing significantly reduces the visibility of the off-diagonal peaks representing the coherent coupling between the different trion states.

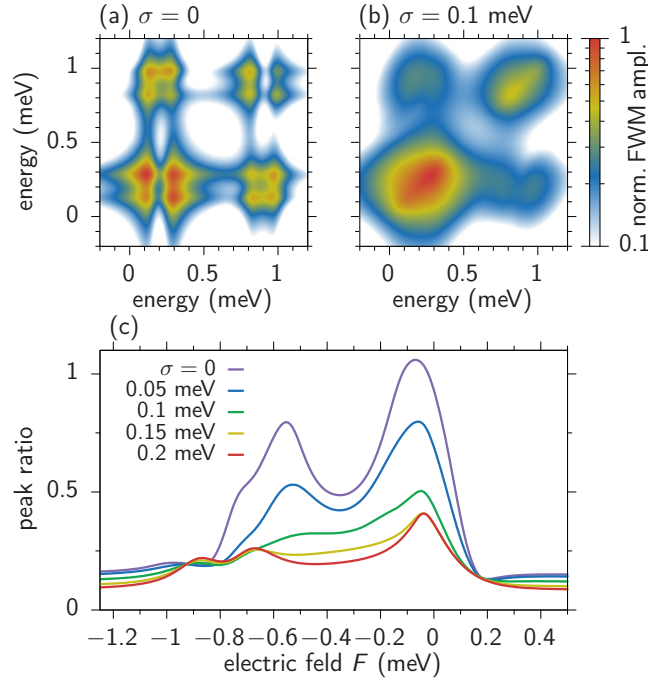


Figure S11: Impact of the inhomogeneous dephasing. (a) 2D FWM with $\sigma = 0$ at an electric field of $F = 0$. (b) Same as (a) but for $\sigma = 0.1$ meV. (c) Simulated peak ratio curves for different inhomogeneous broadenings.

S2E. $\mathbf{k} \cdot \mathbf{p}$ model

Our $\mathbf{k} \cdot \mathbf{p}$ model describes a vertically aligned QDM formed by InGaAs in a GaAs matrix. Both QDs are modeled as lens-shaped with the geometry of the bottom QD being set to 18.0 nm in diameter and 4.0 nm in height, while for the top QD it is 22.0 nm and 4.4 nm, respectively. The dots are separated by a distance of 8 nm (base to base) and they are placed on 0.6 nm thick wetting layers (WLs). Note, that all the values are subject to discretization with a mesh adjusted to 0.565325 nm, which is the lattice constant of GaAs at low temperatures. The maximum In content in the dots and in the WL is 45% with a gradual decrease of indium at the edges, which simulates material intermixing. This is done by processing the composition profile with a Gaussian blur with a standard deviation of 0.6 nm.

We calculate single-particle electron and hole states using an eight-band $\mathbf{k} \cdot \mathbf{p}$ model with the envelope function approximation [12, 13]. The strain which arises due to the lattice mismatch of InAs and GaAs is determined by the continuous elasticity approach [14]. The piezoelectric field is included up to the second order in polarization [15, 16], using parameters from Ref. [17]. Details of the model are given in Ref. [18] with further improvements of Ref. [19]. The trion states are calculated using the configuration-interaction (CI) method, where we consider a basis of 4 electron and 8 hole single-particle states. The electric field is accounted for at the stage of the exact diagonalization of the CI Hamiltonian [20] (with the matrix elements calculated in the basis of single-particle states obtained at zero electric field). The electron-hole exchange is also included at the CI stage. The relevant matrix elements are calculated by mesoscopic expansion of the Coulomb interaction up to second order as in Ref. [21]. We then estimate the atomic integrals using rescaled hydrogen-like wave functions [22] with the effective value of the dielectric constant for local (on-site) integrals being equal to 4. The single- and three-particle eigenstates are then used to compute the amplitudes of the optical transitions [23].

The PL and FWM spectra obtained from the $\mathbf{k} \cdot \mathbf{p}$ modelling are shown in Fig. S12. Qualitatively, in spite of the much richer basis, the $\mathbf{k} \cdot \mathbf{p}$ approach yields the same features in the PL, as the phenomenological model, including the hole and trion resonances as well as the characteristic crossing of transition lines. The FWM spectrum also has exactly the same structure, showing essentially two horizontal branches interrupted by avoided-crossings and with intensities decaying in the opposite directions. Quantitatively, the energy scale (which is determined by the Coulomb correlation energies of the three-particle system) is larger in our $\mathbf{k} \cdot \mathbf{p}$ simulation because of a smaller inter-dot distance, which turned out to be necessary to guarantee the stability of the relevant states in the absence of the AlGaAs barrier in our simplified geometry of the model. One additional feature in the

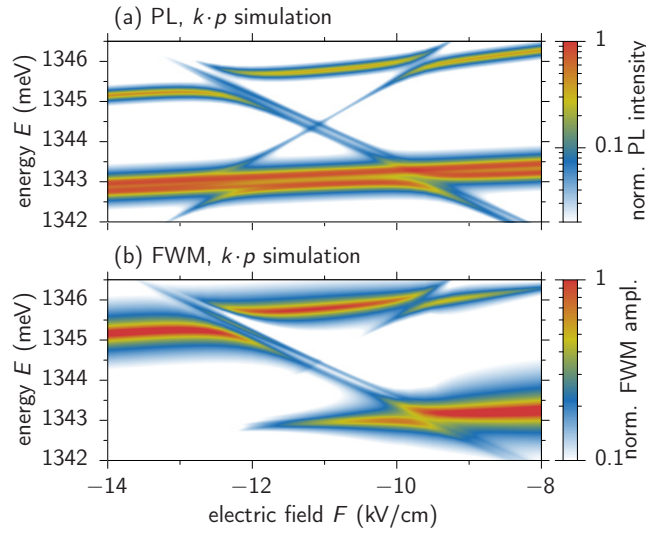


Figure S12: The luminescence (a) and FWM (b) spectra simulated using the system states obtained from the $\mathbf{k} \cdot \mathbf{p}$ model.

$\mathbf{k} \cdot \mathbf{p}$ -based PL spectrum is the line at about 1343 meV that crosses all other transition lines without any interaction (avoided-crossing). This line belongs to a transition between states with an excited hole, i.e., electron-hole recombination in the presence of a spectator hole in an excited state (in the p-shell). It is visible in our PL simulation, where all the trion states are assumed to be equally occupied. This is consistent with the measurements shown in Fig. S6, where a similar line becomes pronounced at higher excitation powers. There is no corresponding line in the FWM spectrum, since this is a resonantly excited coherent measurement in which only the lowest hole states are involved.

References

1. Langbein, W. & Patton, B. Heterodyne spectral interferometry for multidimensional nonlinear spectroscopy of individual quantum systems. *Opt. Lett.* **31**, 1151 (2006).
2. Kasprzak, J., Patton, B., Savona, V. & Langbein, W. Coherent coupling between distant excitons revealed by two-dimensional nonlinear hyperspectral imaging. *Nat. Photonics* **5**, 57–63 (2011).
3. Fras, F. *et al.* Multi-wave coherent control of a solid state single emitter. *Nat. Photonics* **10**, 155 (2016).
4. Hahn, T. *et al.* Destructive photon echo formation in six-wave mixing signals of a MoSe₂ monolayer. *Adv. Sci.* **9**, 2103813 (2022).
5. Schall, J. *et al.* Bright electrically controllable quantum-dot-molecule devices fabricated by in situ electron-beam lithography. *Adv. Quantum Technol.* **4**, 2100002 (2021).
6. Wigger, D. *et al.* Acoustic phonon sideband dynamics during polaron formation in a single quantum dot. *Opt. Lett.* **45**, 919–922 (2020).
7. Wigger, D. *et al.* Exploring coherence of individual excitons in InAs quantum dots embedded in natural photonic defects: influence of the excitation intensity. *Phys. Rev. B* **96**, 165311 (2017).
8. Mermillod, Q. *et al.* Harvesting, coupling, and control of single-exciton coherences in photonic waveguide antennas. *Phys. Rev. Lett.* **116**, 163903 (2016).
9. Wigger, D. *et al.* Rabi oscillations of a quantum dot exciton coupled to acoustic phonons: coherence and population readout. *Optica* **5**, 1442–1450 (2018).
10. Hahn, T., Kasprzak, J., Machnikowski, P., Kuhn, T. & Wigger, D. Influence of local fields on the dynamics of four-wave mixing signals from 2D semiconductor systems. *New J. Phys.* **23**, 023036 (2021).

11. Siemens, M. E., Moody, G., Li, H., Bristow, A. D. & Cundiff, S. T. Resonance lineshapes in two-dimensional Fourier transform spectroscopy. *Opt. Express* **18**, 17699–17708 (2010).
12. Bahder, T. B. Eight-band $\mathbf{k}\cdot\mathbf{p}$ model of strained zinc-blende crystals. *Phys. Rev. B* **41**, 11992 (1990).
13. Winkler, R. *Spin-Orbit Coupling Effects in Two-Dimensional Electron and Hole Systems* (Springer, 2003).
14. Pryor, C., Kim, J., Wang, L. W., Williamson, A. J. & Zunger, A. Comparison of two methods for describing the strain profiles in quantum dots. *J. Appl. Phys.* **83**, 2548 (1998).
15. Bester, G., Zunger, A., Wu, X. & Vanderbilt, D. Effects of linear and nonlinear piezoelectricity on the electronic properties of InAs/GaAs quantum dots. *Phys. Rev. B* **74**, 081305(R) (2006).
16. Bester, G., Wu, X., Vanderbilt, D. & Zunger, A. Importance of second-order piezoelectric effects in zinc-blende semiconductors. *Phys. Rev. Lett.* **96**, 187602 (2006).
17. Caro, M. A., Schulz, S. & O'Reilly, E. P. Origin of nonlinear piezoelectricity in III-V semiconductors: Internal strain and bond ionicity from hybrid-functional density functional theory. *Phys. Rev. B* **91**, 075203 (2015).
18. Gawarecki, K. Spin-orbit coupling and magnetic-field dependence of carrier states in a self-assembled quantum dot. *Phys. Rev. B* **97**, 235408 (2018).
19. Krzykowski, M., Gawarecki, K. & Machnikowski, P. Hole spin-flip transitions in a self-assembled quantum dot. *Phys. Rev. B* **102**, 205301 (2020).
20. Świdorski, M. & Zieliński, M. Exact Diagonalization Approach for Atomistic Calculation of Piezoelectric Effects in Semiconductor Quantum Dots. *Acta Phys. Pol. A* **129**, 79–82 (2016).
21. Azizi, M. & Machnikowski, P. Interband Coulomb coupling in narrow-gap semiconductor nanocrystals: $\mathbf{k} \cdot \mathbf{p}$ theory. *Phys. Rev. B* **91**, 195314 (2015).
22. Karwat, P., Gawarecki, K. & Machnikowski, P. Phonon-assisted carrier tunneling with hyperfine-induced spin flip in coupled quantum dot systems. *Phys. Rev. B* **104**, 045308 (2021).
23. Gawęlczyk, M. *et al.* Exciton lifetime and emission polarization dispersion in strongly in-plane asymmetric nanostructures. *Phys. Rev. B* **96**, 245425 (2017).